ISSN 0016-8521, Geotectonics, 2018, Vol. 52, No. 2, pp. 209–224. © Pleiades Publishing, Inc., 2018.
Original Russian Text © D.S. Nikitin, P.P. Gorskikh, M.D. Khutorskoy, D.A. Ivanov, 2018, published in Geotektonika, 2018, No. 2, pp. 58–75.

Structural–Tectonic Features of the Northeastern Barents Plate from Numerical Modeling of Potential Fields

D. S. Nikitin[a, *], P. P. Gorskikh[b], M. D. Khutorskoy[a], and D. A. Ivanov[c]

[a]*Geological Institute, Russian Academy of Sciences, Moscow, 119017 Russia*
[b]*OOO Noril'skgeologiya, OJSC MMC Norilsk Nickel, Norilsk, 663300 Russia*
[c]*Voronezh State University, Voronezh, 394006 Russia*
**e-mail: ndsnomination@mail.ru*

Received January 25, 2017

Abstract—Structural–geological inhomogeneities in the northeastern Barents Sea are zoned based on an analysis of various components of the gravity and magnetic fields. The objects revealed in the basement and sedimentary cover of the Barents Sea Plate form anomalies in potential fields at coexisting complex geological structures and contrasting petrophysical properties. Cluster analysis reveals the fault-marked boundaries of individual blocks in the basement. A numerical model of faults in the sedimentary cover and basement of the Barents Sea Plate is constructed.

Keywords: Barents Sea Plate, basement, sedimentary cover, potential fields, intrusion, numerical modeling

DOI: 10.1134/S0016852118020085

INTRODUCTION

On the northeastern Barents Sea shelf, a large amount of geological and geophysical works have been being carried out in the last decade to clarify the regional petroleum potential.

The article presents the results of detailed analysis and modeling of gravity and magnetic fields, along with the seismogeological data involved, to solve certain problems of predicting the location and depth of hydrocarbon fields.

The basis for modeling using such parameters as velocity, density, and magnetization was data obtained by the authors during geophysical works (including seismic profiling and gravity and magnetic surveys) conducted by OAO Marine Arctic Geological Expedition, Murmansk, Russia (OAO MAGE) in 2006–2010 on the northeastern Barents Sea shelf. The new data obtained by the authors gave grounds to update the current interpretations of the deep structure of the northeastern Barents Sea and elaborate them in detail. In the present paper, the new results are presented on structural–tectonic zoning of the water area and adjacent islands, obtained by numerical modeling of potential fields.

The studied water area is located in the northeastern Barents Sea, between the Novaya Zemlya archipelago and Franz Josef Land. In terms of the character of seismic records and distribution of potential geophysical fields, it can be subdivided into two parts: northwestern and southeastern (Fig. 1). The northwestern part includes the East Barents megatrough, while the southeastern part is represented by the Fore-Novaya Zemlya structural zone (formed by the Admiralteistva, Pankrat'ev, and Cape Zhelaniya rises) and also by such troughs as the Sedov, Mack, Gulfstream, and Karpov (Fig. 1). The East Barents megatrough, filled with Middle Paleozoic–Mesozoic rocks, has a sedimentary cover 18–20 km thick. The consolidated crust is from 10 to 15 km here; the Moho occurs at a depth of 27–33 km. The crust is thinned due to the absence of a granite-gneiss layer [23]. The main tectonic faults in the basement of the East Barents megatrough are NE- and NW-trending and are characterized as transform faults with a right-lateral strike-slip component.

Transiting from the East Barents megatrough to Fore-Novaya Zemlya structural zone, such parameters as the crustal structure, shape of potential field anomalies, and character of magmatism abruptly change. The basement surface rises southeastward in stepwise manner: it is composed of blocks raised to different levels; these blocks have also been disintegrated and thrusted to the crystalline basement of the East Barents megatrough. Crustal thickness increases to 36–38 km, but the thickness of the sedimentary cover and granitic-metamorphic layer vary considerably.

The boundary between the East Barents megatrough and the Fore-Novaya Zemlya structural zone is traced along deep fault zones. In the central part of the studied region, it is expressed in the magnetic field as a broad (40–80 km wide) linear NE-trending negative

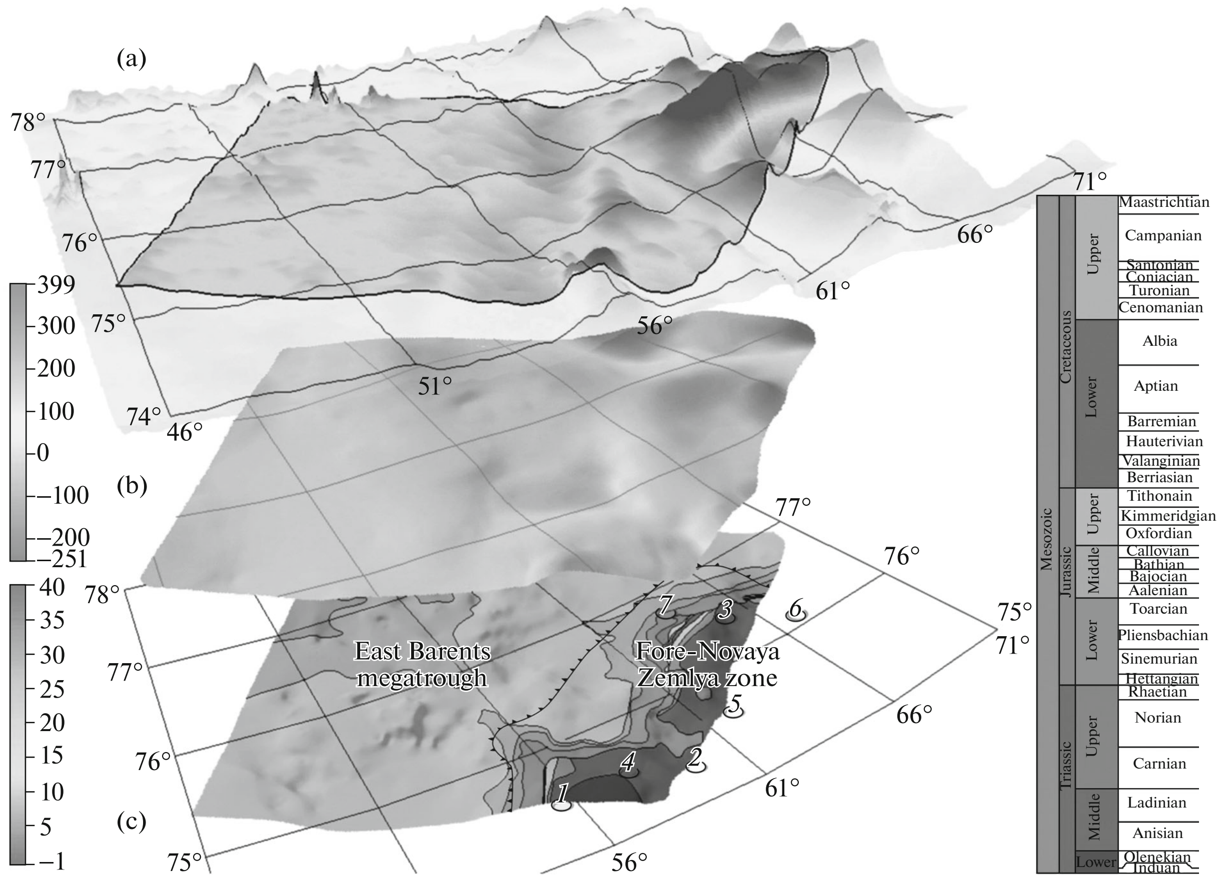

Fig. 1. Maps of anomalous magnetic (a) and gravity (b) fields and geological map of pre-Quaternary rocks (c). Arbitrary notes: (*1*–*3*) uplifted crustal blocks: (*1*) Admiralteistva, (*2*) Pankrat'ev, (*3*) Cape Zhelaniya; (*4*–*7*) sunken crustal blocks: (*4*) Sedov, (*5*) Mack, (*6*) Gulfstream, (*7*) Karpov.

anomaly (Fig. 2). Within this zone, NE-trending and submeridional thrusts traced from the Novaya Zemlya orogen are replaced by NE-trending normal faults. On the eastern side of the East Barents megatrough, sinking of blocks of the Fore-Novaya Zemlya structural zone can be seen. The temporal cross sections of this structural zone clearly demonstrate the presence of large intrusions whose upper margins occur at depths of 8–10 km.

STRUCTURES OF THE BASEMENT AND SEDIMENTARY COVER

In the mid-1980s, after the first gravimagnetic studies were conducted, a schematic of structural–tectonic zoning was developed for the region to show the principal difference in structures of the western and eastern parts of the Barents Sea Plate. Note that this schematic has not been significantly revised until present [17].

Before geophysical gravimagentic works were started, ideas about the Barents Sea structure were based on geological data from adjacent islands [19].

It was proven that detrital material flow in the Ordovician–Devonian on the Northern Island of Novaya Zemlya took place from the northwest [5]. Based on this knowledge, the continuation of the Grampian geosyncline (i.e., continuation of the Norwegian Caledonides) in the Barents Sea was demonstrated. The Novaya Zemlya archipelago and Admiralteiskii Swell, with a well-developed granitic-metamorphic layer but thin sedimentary cover, were considered as the eastern terminus of the East Barents megatrough [16].

The eastern part of the Barents Sea Plate is represented by the East Barents megatrough, which consists of several basins divided by rises. It was found that the thickness of the sedimentary cover in it is up to 18 km, while there is no granitic-metamorphic layer; the crustal thickness is 20–25 km [14].

The western part of shelf is characterized by a thinned sedimentary cover, cut relief of the basement, and a number of isometric rises (entral Barents, Persei, Franz Josef Land) with linear troughs between them.

The most disputable problem for the East Barents megatrough has always been that regarding its age and formation mechanism. The rifting hypothesis was developed for the first time by M.L. Verba [6]. By analogy with West Siberian rifts, it was supposed that the East Barents rift formed at the Permian–Triassic boundary [6]. However, as the extent of seismic methods increased in depth, it was revealed that the Permian–Triassic terrigenous sequence covers thick Paleozoic deposits, which appeared to significantly differ from the overlying sequence in terms of the wave field.

The first geophysical investigations using the seismic reflection method revealed clinoforms in the upper part of the cross section, while in the lower part, they revealed well-traced horizontal reflectors, which are usually characteristic of carbonate deposits in continental platforms.

The continental platform concept contradicted the deep structure of the megatrough, namely, the absence of a granite-metamorphic layer, which is an obligatory feature of all continental platforms. However, the revised rifting model showed no contradiction with the deep structure under the assumption that the trough had a thick upper crust and divergence of the sides of the trough, which resulted in exposure of the lower crust to the surface [3]. The model of Permian–Triassic rifting in the East Barents megatrough is discussed in [9, 11, 16] and is still valid today.

A Devonian age of rifting was inferred from the interpretation of linear magnetic anomalies [1, 3, 20]. However, these assumptions do not agree with the results of geological surveys on Barents Sea islands: no continuation of a rift was found for which the width of the opening pole should have been located much further south with respect to the contemporary position of the Barents Sea.

Drilling on the southern side of the South Barents Basin and on Kolguyev Island has recovered Upper Cambrian marine terrigenous deposits [14] absent in the majority of the Timan–Pechora zone (apart from the Near-Timan area), in the Pai-Khoi Range (central Yugra Peninsula), and on Southern Island of Novaya Zemlya [25]. According to seismic data [8], there is a sedimentary cover (Cambrian and probably Precambrian) about 3 km thick beneath them, supporting the idea that the thickness of the sedimentary cover increases northwards, from Kolguyev Island to the South Barents Basin. Since the Timan–Pechora zone was a provenance area until the late Ordovician and only then sank underwater, Riphean–Cambrian deposits can be found at the base of the sedimentary cover in the South Barents Basin.

Unambiguous and interpretable data were obtained on the eastern side of the North Barents Basin [18]. In the northern block of Northern Island (Novaya Zemlya archipelago), a thick sequence of terrigenous deposits is exposed. Its lower part is represented by deep-water sediments containing hardly any benthic fossils; its thickness is 10 km or more, with the pre-Paleozoic part being at least 3 km thick. Some horizons contain fragments of limestone, sandstone, granitoids, and quartz. Multiple traces of landslides suggested a northern or northwestern location of the eroded area.

It remains unclear whether the North Barents Basin and southwestern Franz Josef Land were the transitional zone for detrital material or the entire complex of Riphean–Paleozoic deposits was detached along the basement–cover interface and moved southeastward to occupy its contemporary position in the northern Novaya Zemlya archipelago. If this did happen, it should have occurred in the post-Permian time, because the allochthon in the North Novaya Zemlya zone contains Upper Permian (Tatrian) deposits. In this scenario, the present-day North Barents Basin could not have Early and Middle Paleozoic deposits, with onset of sedimentation as late as the Triassic.

Thus, the data on the northern block of Northern Island (Novaya Zemlya archipelago), the East Barents megatrough, and the Admiralteiskaya borehole indicate that the megatrough formed as a unified structure with oceanic crust by the beginning of the Paleozoic [4].

Significant transformations in the Paleozoic were reported only in the western and northern margins of the plate, where they were caused by processes in the adjacent oceanic basins, e.g., the Japetus Paleoocean and Atlantic Ocean (in the Paleozoic and Late Mesozoic–Cenozoic, respectively) to the west of it, and some oceanic basin that probably existed in the north (in contemporary coordinates), north of the present-day Lomonosov Ridge. Until the Cenozoic, it was the part of the Svalbard Platform. Beginning from the Paleocene (65 Ma ago), the Eurasian Basin became the northern boundary of the Svalbard Platform.

REGULAR PATTERNS OF CHANGES IN PHYSICAL PROPERTIES OF SEDIMENTARY ROCKS ON THE BARENTS SEA SHELF

Drilling of deep stratigraphic wells on the Barents Sea islands made it possible to characterize the entire cross section of the sedimentary sequence from the Proterozoic to the Paleogene. Five boreholes in the northern Barents Sea characterized different parts of the cross section.

(1) Nagurskaya borehole (Alexandra Land, Franz Josef Land, 3204 m depth, drilled in 1977). The recovered sedimentary rock ranged from Carboniferous terrigenous deposits to Triassic and Cretaceous siltstones and argillites; in the lower parts of the sequence, metamorphic rocks of the Late Proterozoic (Vendian) folded basement were recovered.

(2) Heiss borehole (Heiss Island, Franz Josef Land, 3344 m depth, drilled in 1981). The sequence of Triassic deposits was characterized: these were silty-

clayey rocks with inclusions of gabbro-dolerite intrusions.

(3) Northern borehole (Graham Bell Island, eastern Franz Josef Land, 3528 m depth, drilled in 1979). The recovered deposits of Triassic were sandy-silty and clayey-silty with interbeds of carbon-bearing rocks and coal lenses, as well as also dolerite intrusive bodies.

(4) Grumant borehole (Spitsbergen Island of Svalbard, 3173 m depth, drilled in 1975) recovered a sequence from the Paleogene to the Permian, including the entire Mesozoic interval.

(5) Raddedalen-1 borehole (Edgeøya Island, southeast Svalbard, 2828 m depth, drilled in 1971) recovered Upper Permian limestones, as well as Lower Carboniferous limestones, dolomites, and sandstones; and Middle–Upper Carboniferous limestones and dolomites with argillite interbeds.

Comparison of the results of measuring the physical properties of core samples from these wells and those in logging diagrams revealed several important patterns of how these properties change along the depth and over the area. These patterns can be formulated as follows:

(1) the density of sedimentary rocks varies from 1.78 to 2.94 g/cm^3, the density of metamorphic rocks varies from 2.67–2.77 g/cm^3, and the density of erupted rocks varies from 2.80–3.10 g/cm^3;

(2) the density in the series sandstones–siltstones–argillites increases from 1.78 to 2.80 g/cm^3, depending on the clay content in rock;

(3) the density of carbonate varieties vary from 2.50 (limestones) to 2.90 g/cm^3 (dolomites);

(4) anhydrites are characterized by maximal density values (2.90–2.95 g/cm^3).

Catagenesis is the leading factor affecting the density of terrigenous rocks. It was found that the longitudinal wave velocity regularly increases along with density in both terrigenous and carbonate rocks as temperature and pressure increase.

The longitudinal wave velocity in terrigenous deposits varies from 2.0 to 5.0 km/s; in metamorphic rocks, from 5.0 to 6.0 km/s; in carbonate and erupted rocks, from 5.0 to 6.5 km/s. The revealed regional density benchmarks are in the same time seismic ones. The most contrasting interface in the cross section of the shelf is the boundary between the Mesozoic (terrigenous) and Paleozoic (carbonate) complexes. An excessive density and velocity jump at the base of sedimentary rocks and at the boundary with the Archean–Proterozoic crystalline basement is so sharp everywhere that the basement surface can be mapped using gravity and seismic survey data. The relief of the basement surface is the main structure-forming factor on the entire polar shelf, which is characteristic of all passive continental margins.

The magnetic susceptibility of sedimentary rocks in core and sludge samples is characterized by values of 0–50 × 10^{-5} SI, rarely, to 80 × 10^{-5} SI. Siderite nodules are more magnetic, with 180 × 10^{-5} SI.

The rocks of the sedimentary sequence are believed to be nonmagnetic. However, there is a weak but stable tendency for magnetization to increase with depth, which can be explained by catagenetic processes. The magnetic susceptibility varies from 10 × 10^{-5} to 50 × 10^{-5} SI.

Erupted rocks (dolerites, basalts) have magnetic susceptibility of about 1500–1700 × 10^{-5} SI, rarely 100–300 × 10^{-5} SI.

Heat flow in the studied wells is above the average level for Earth (55–65 mW/m^2), suggesting that the region is tectonically active at present and there are mantle sources of heat [29].

A characteristic feature of erupted rocks from boreholes is their high remanent magnetization, which exceeds the value of induced magnetization by a factor of 5–18, with the remanent magnetization vector coinciding in direction with the present-day terrestrial magnetic field. Basalts demonstrate a high magnetite content (1–5%) with a high remanent magnetization and high Curie temperature (530°–570°C). These magnetic properties are characteristic of all erupted rocks of the Paleozoic and Mesozoic.

Thus, based on all magnetic properties of erupted rocks (basalts, diabases, dolerites), we can conclude that they formed from deep sources; the drilling data suggest that erupted rocks intruded in the Late Triassic and probably later.

POTENTIAL FIELD INTERPRETATION METHOD

The potential fields were analyzed using the filtering technique based on fast Fourier transform (FFT). Transforming the gravimagnetic data into the Fourier space, we can treat them as a function of the wavenumber or wavelength. Such a form of data representation implies a number of operations that can be used to obtain the desired information, to remove undesired information, or to transform the data (determination of a trend or vertical derivative, analytical continuation of the field, etc.).

Calculation of potential field transforms makes it possible to model the positions of magnetic contact surfaces attributed to the boundaries of geological objects [31, 33, 34, 36].

The structures of gravity and magnetic fields form owing to the superposition of anomalies having different origins, caused by density (in the case of gravity field) and magnetic inhomogeneities of geological bodies. They have different lateral extents, different amplitudes of physical properties with respect to the background values, and different occurrence depths of anomaly-forming objects. It is these factors that explain the appearance of both regional and local anomalies.

Subdivision into these two types of anomalies is determined by the scale of studies. Detailed large-scale surveys within the limits of shelf plates demonstrate that regional anomalies differ from local ones only in the depth of the source, although both fit the contrast objects in the sedimentary cover. Studies of long geotraverses or small-scale areal surveys are able to classify the regional anomalies formed by basement inhomogeneities. On this background, smaller (local) anomalies are usually located in the sedimentary cover.

The existing borehole-tested methods of potential field transformation make it possible to filter deep regional and near-surface local anomalies, and the choice of the transforming algorithm yields a tomographic section of anomalous field at different depths.

The most frequently used potential field transformation methods are averaging, analytical continuation (transformation) of the field to the upper or lower half-space, and calculation of the higher derivatives of the potential. The Δg and ΔT fields of anomalies taken, e.g., along some profile are complex curves reflecting the overlapping mutual influence of various bodies occurring at different depths in the crust. Moving away from or approaching anomalous masses, will therefore weaken or strengthen, respectively, certain anomalies because the values of the gravity and magnetic field potentials are inversely proportional to the distance to a disturbing object. The gravity and magnetic potentials are harmonic functions; i.e., they change weakly with small increases in argument and they are repeatedly differentiable.

The field produced by deeply seated large geological bodies is weakly variable by transformations. Recalculating either the Δg or ΔT field to the upper half-space, we largely exclude the effects from local structures and emphasize the field produced by large objects of regional scale. On the other hand, recalculating the observed field to the lower half-space (for example, to the level of crystalline basement), we largely intensify the local anomalies produced by small shallow (near-surface) objects. Thus, transform procedure is analogous to filtering: in the case of upward continuation, high-frequency components of Δg and ΔT curves are suppressed, while low-frequency ones are emphasized; at downward continuation, vice versa, high-frequency background of anomalies intensifies with the simultaneous relative decrease in low-frequency ones. The effect analogous to continuation to the upper half-space is produced by averaging of the filed with respect to areas. Calculation of higher derivatives of Δg and ΔT, like the borehole is recalculated to the lower half-space, strengthens the high-frequency field components. Thus, knowing the distribution of Δg or ΔT on the land or water surface, we can calculate their values above or below this surface.

It should be noted that recalculation to the lower half-space leads to a considerable increase in the effect from measurement errors. To reduce these errors, we preliminarily smoothed the Δg or ΔT curve at each recalculation level. Of course, these procedures distort the initial data and cause false anomalies (or vice versa, they hide the existing ones); therefore, the transform procedures can be effectively performed when high-precision observations.

The applied modeling method implies (1) iterative solution of the direct problem (calculation of the gravimagnetic effect from the supposed geological section) and (2) creation of a density–magnetic model of the crustal structure along the profile for which the model gravity and magnetic fields demonstrate the best fit to the observed one. This makes it possible to interpolate the position of the density and magnetic boundaries at sites where factual data are either absent or unreliable.

The density of deep layers was estimated from the known ratios between the density and longitudinal wave velocity. In addition, we employed petrophysical data obtained from cores from wells on Franz Josef Land [28, 30].

The calculations were done using the OASIS MONTAJ package (Geosoft Software, Canada) [38].

Modeling and analysis of the potential fields made it possible (i) to reliably determine the structure, material composition, and geodynamic conditions of crust formation, (ii) to verify the manifestations of intrusive magmatism and salt diapirism, (iii) to trace tectonic elements that are clearly reflected in the potential fields, and (iv) to refine the deep structure of the Earth's crust.

DISCUSSION

For a geophysical characterization of the northeastern Barents Sea shelf, we compiled maps of anomalous magnetic and gravity fields (Figs. 2, 3). The detailed characteristics of geological complexes reflected in the potential fields were obtained by calculating their local components (Figs. 4, 5).

The local components of the potential fields were calculated by the MAGMAP module of the OASIS MONTAJ software [38] by finding the radially averaged energy spectrum of the potential fields (based on 2D FFT) and by filtering the obtained energy spectrum with the Gaussian Regional/Residual Filter. This is a smoothing filter often used to distinguish high- or low-frequency field components. The theoretical basics of 2D FFT application are discussed in [31, 32, 35, 37].

Figures 6 and 7 show the radially averaged energy spectrum for the magnetic and gravity fields, respectively. The top panels (Figs. 6a, 7a) show the averaged

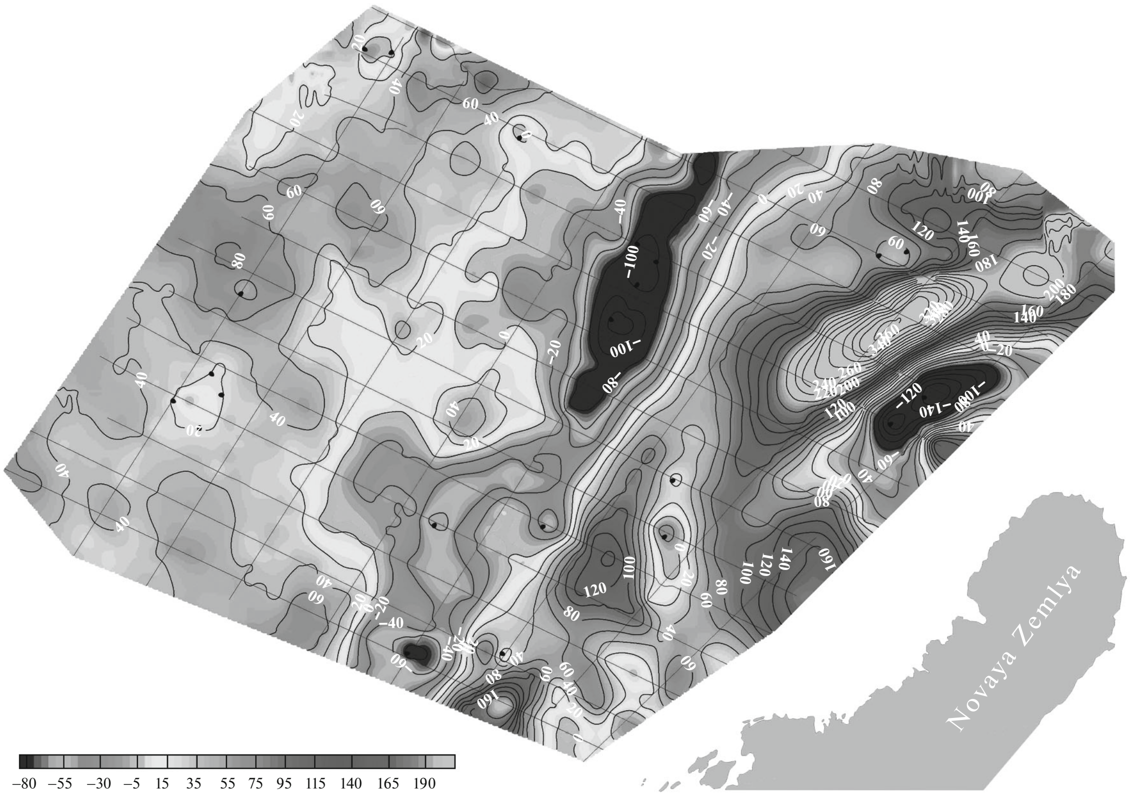

Fig. 2. Map of anomalous magnetic field on northeastern Barents Sea shelf.

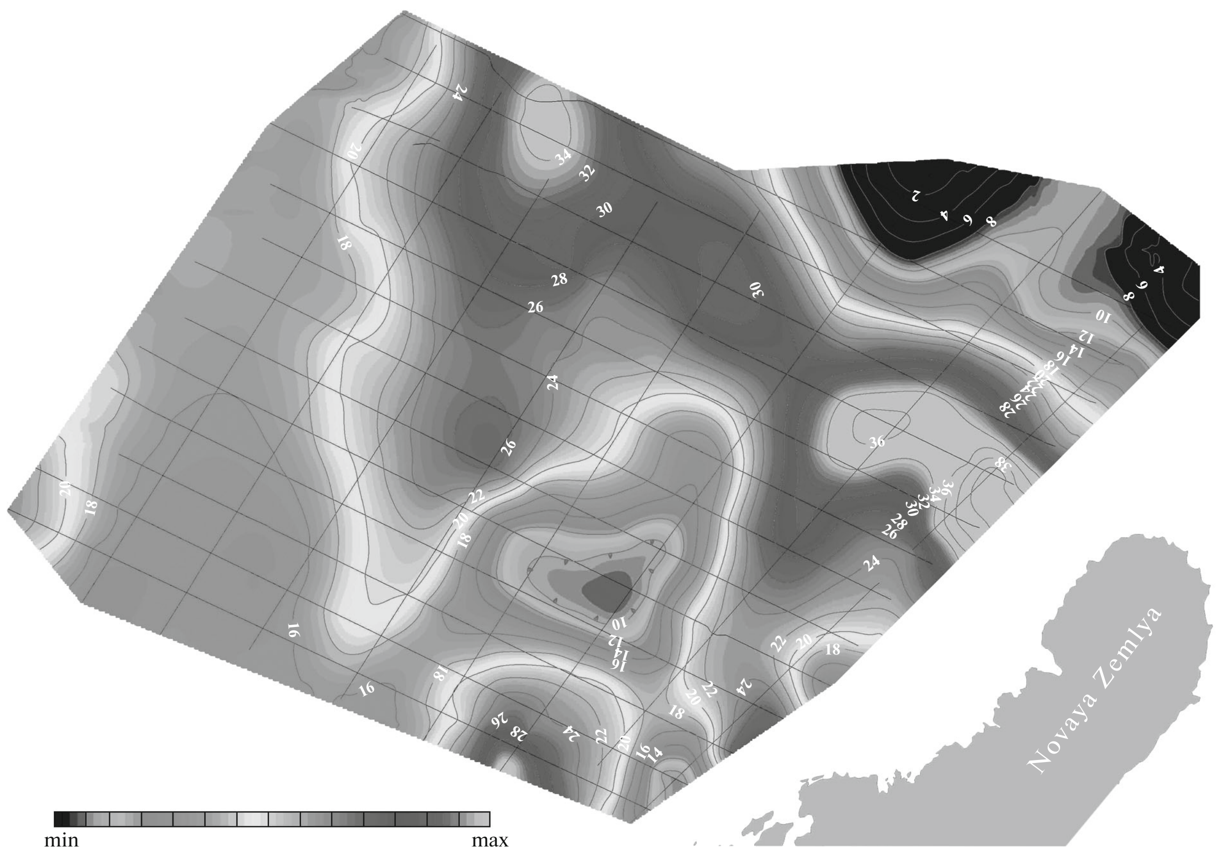

Fig. 3. Map of Bouguer gravity field for intermediate layer density of 2.67 g/cm^3 on northeastern Barents Sea shelf.

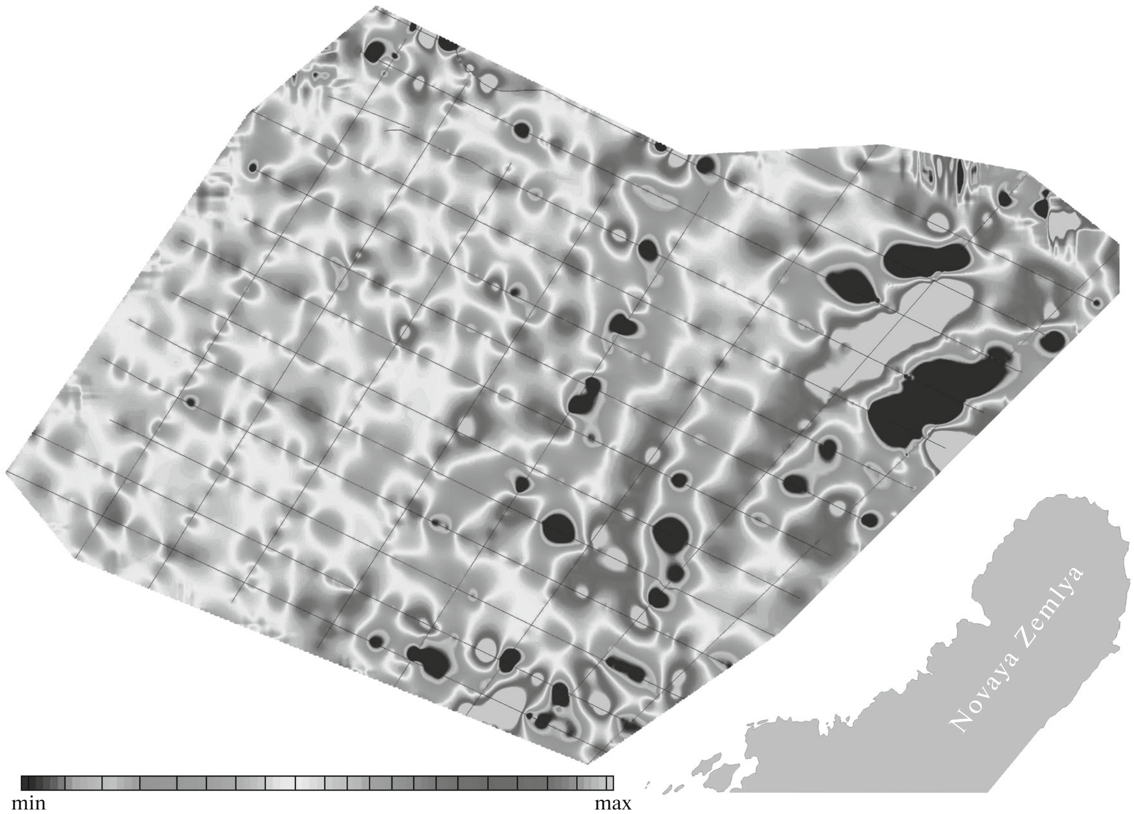

Fig. 4. Map of local component of anomalous magnetic field on northeastern Barents Sea shelf.

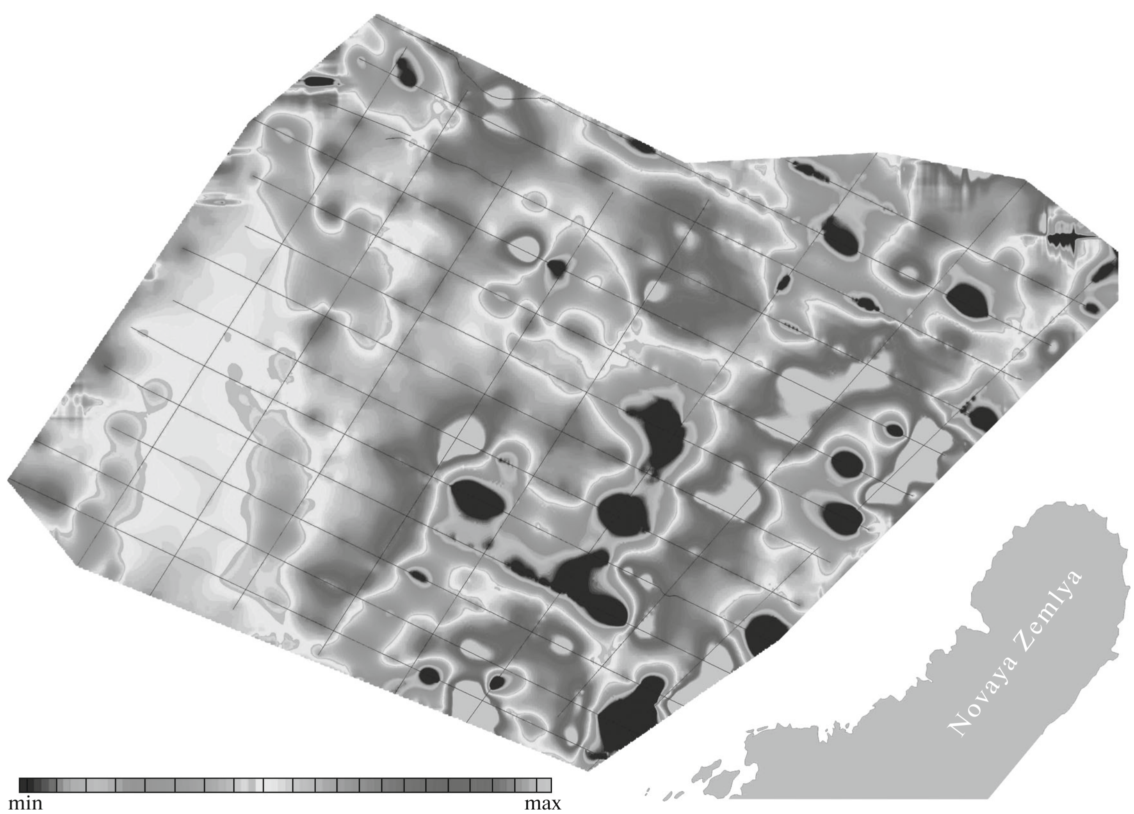

Fig. 5. Map of local component of anomalous gravity field on northeastern Barents Sea shelf.

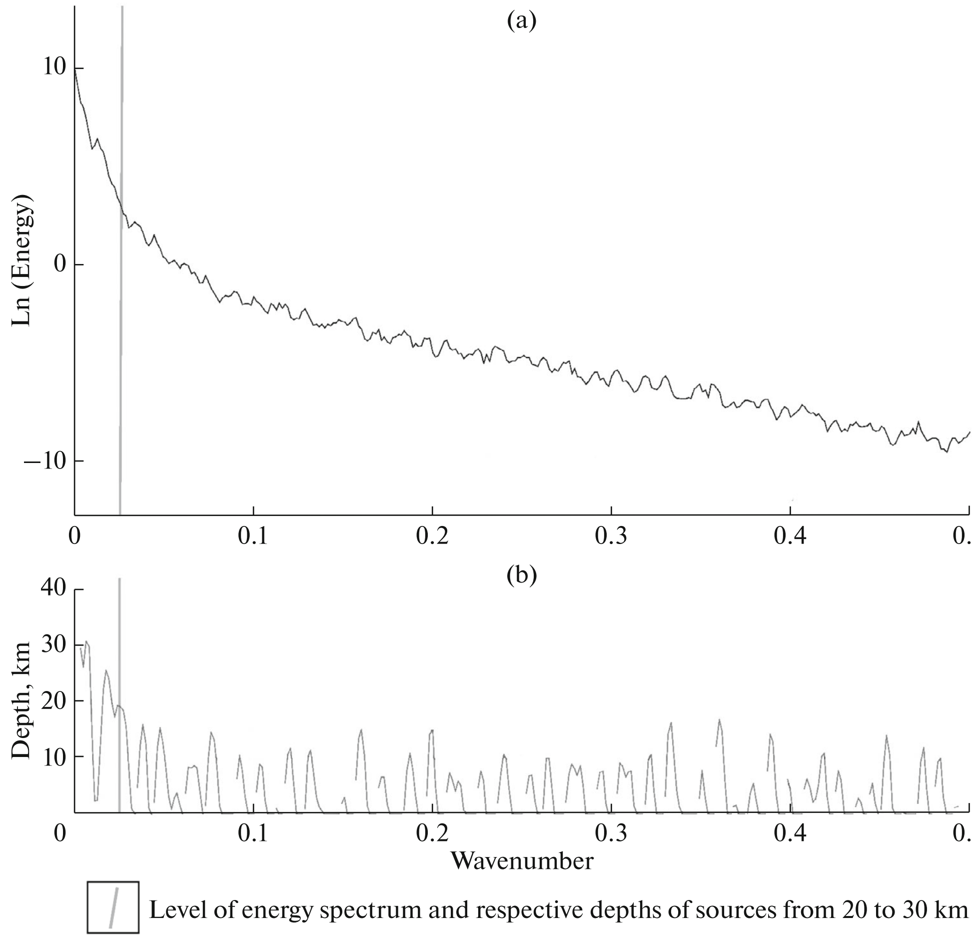

Fig. 6. Radially averaged energy spectrum of magnetic field (a) and curve of depth of upper special point (b).

energy, which is the spectral density averaged for all grid elements for the corresponding wavenumber; the bottom panels (Figs. 7, 8) show the estimated depths of field sources, obtained from the slope angles in the energy spectrum. The depth to the statistical set of sources is determined with the following expression:

$$h = -s/4\pi,$$

where h is depth and s is the slope angle of energy spectrum logarithm.

The obtained estimates can be used as approximate references when determining the depths of field sources. In our case, groups of deep (from 20 to 60 km) and shallow (down to 10–15 km) sources can be distinguished for the gravity field. Analogous groups are also distinguished for the magnetic field: deep ones occur at depths of 20–30 km, and shallow ones, at depths of 10–15 km.

Using the data obtained from analyzing the energy spectra of potential fields, we calculated their local components by filtering the respective energy spectrum for a group of deep sources. Thus, the obtained local components of the magnetic and gravity fields carry information about the spatial distribution of groups of shallow sources (down to 10–15 km). The MAGMAP module [38] makes it possible to change the filter parameters to see the filtering result immediately. For both the gravity and magnetic fields, we chose the value of filter standard deviation (0.02) that would exclude from the initial data the energy spectrum corresponding to groups of deep sources.

Zoning in terms of the geophysical field parameters marked the beginning of the interpretation process. The main problem of zoning is partitioning the area into blocks characterized by values with a homogeneous level and similar features of relationships between input parameters. The boundaries of these blocks usually run along tectonic faults. Thus, the problems of areal zoning and tracing of faults are closely related.

When zoning, we used the set of geophysical fields characterizing the magnetization and density of rocks.

The studied area was zoned by classifying multiparametric digital geophysical data by the K-means method using the COSCAD-3D software package for spectral correlation analysis of 3D geodata [39]. The algorithm in this software partitions the area into clusters with homogeneous levels of values and structures

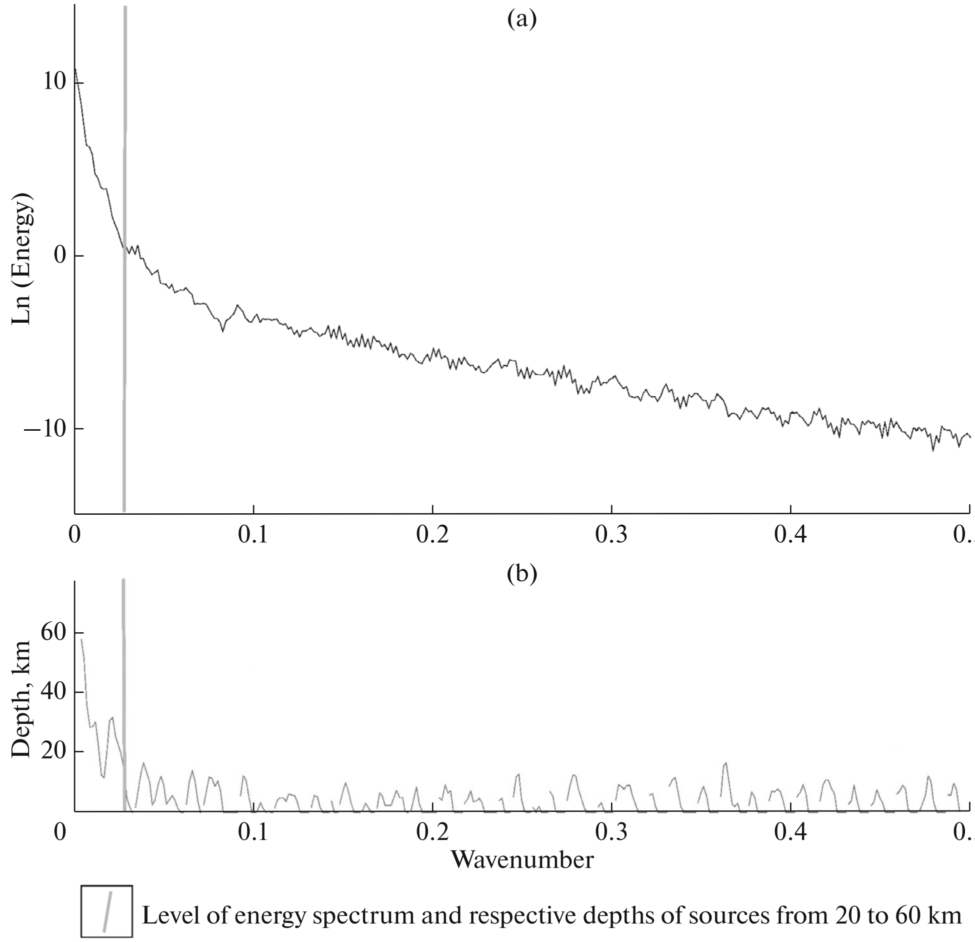

Fig. 7. Radially averaged energy spectrum of gravity field (a) and curve of upper special point depth (b).

of relationships between geophysical parameters. The least dense and nonmagnetic rocks are indicated in light blue and blue, while dense and magnetic units are indicated in red (Fig. 8).

Joint classification of the local component of the magnetic and gravity fields is done in a similar way (Fig. 9). The local component reflects the objects nearest the surface, which in our case corresponds to inhomogeneities in the sedimentary cover, including those related to igneous objects.

Based on joint interpretation and analysis of geological, tectonic, and geophysical data, we revealed the following main geophysical criteria for distinguishing and tracing faults.

(1) Zones of intensive linear horizontal gradients, like magnetic “benches,” were distinguished in the boundaries between blocks; these zones differ in vertical thickness, size, shape, and occurrence depth of the contact surface.

(2) Abrupt changes in directions and shifting of isolines along the course, sharp bends and their narrowing in lateral view, frontal closing or breakage.

(3) Changes in the level, sign, character, and shape of anomalies at the contact between blocks.

(4) Series of sign-alternatingmagnetic anomalies fitting the contact between blocks.

The bedding elements of some contact surfaces were refined by calculating the spatial coordinates of single sources using the Eulerian deconvolution algorithm (Fig. 10). Analysis of the distribution of special points in the potential fields made it possible to specify the ranks, positions, and dipping directions of tectonic fault planes identified from geophysical data.

The potential field was modeled along profile 200705 (Fig. 11). The initial data for constructing the model were the SRM–CDP (seismic reflection method–common depth point) seismic section and data on petrophysical properties of rocks.

At the first calculation stage, we digitized the seismic section and reflectors, which were dynamically expressed in the wave field of discordant horizons of group α (Fig. 11) and attributed to layered igneous intrusions (sills). The nature of these objects was revealed by drilling at the Ludlovskaya-1 borehole, where several gabbro-dolerite layers were recovered at

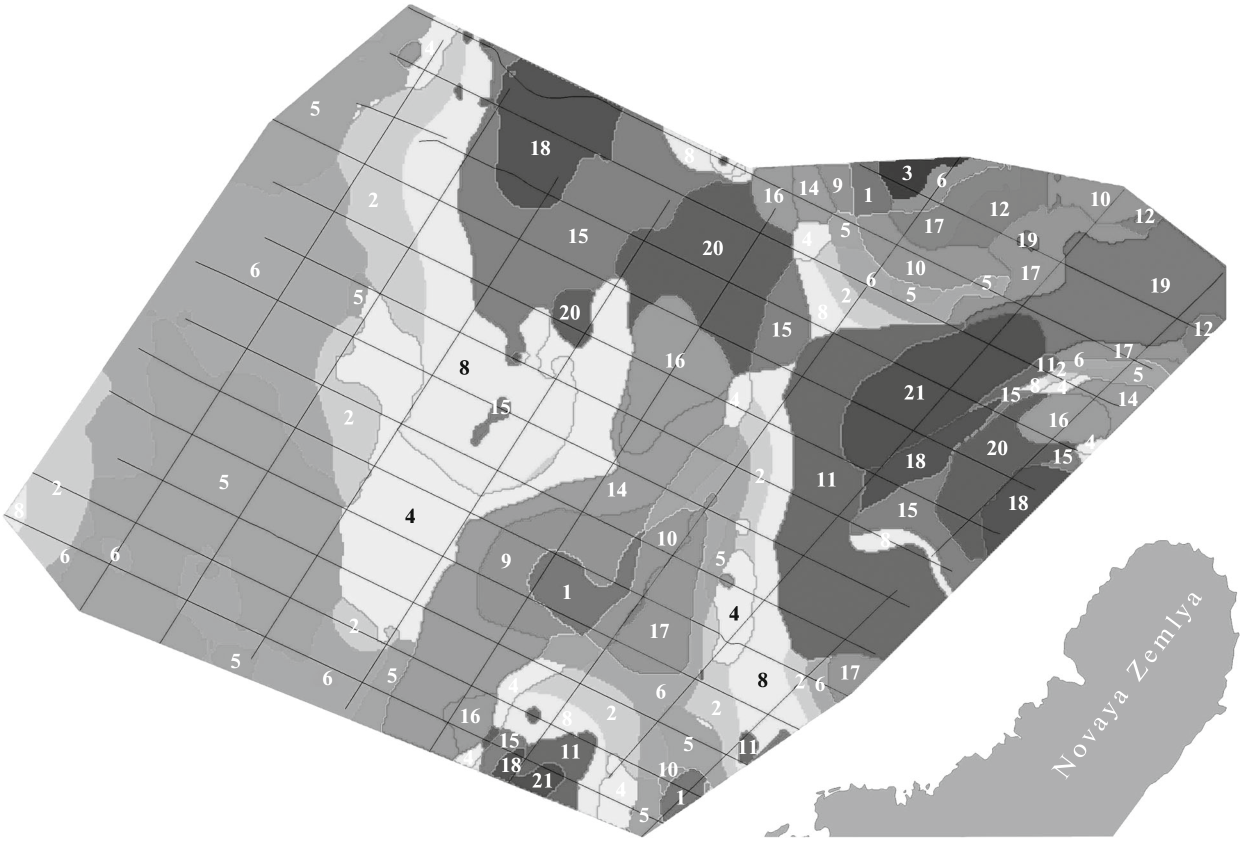

No.	Number of points	Gravity field, mGal		Anomalous magnetic field, nT	
		Mean value	Standard deviation	Mean value	Standard deviation
7	100542	20.37	0.81	38.79	4.89
5	17395	15.88	1.01	28.65	10.91
14	6344	17.23	1.44	–37.46	15.41
9	2695	12.42	1.45	–34.71	16.17
1	1766	9.45	1.32	–3.06	12.66
3	456	2.45	1.32	5.88	14.65
6	15422	16.75	1.08	56.51	12.71
2	419	2.20	1.21	42.47	10.04
10	2846	10.21	1.54	58.35	15.07
17	3910	12.26	2.48	117.67	19.76
13	885	4.19	1.40	66.84	10.68
12	1141	6.69	1.53	106.28	17.67
19	3976	8.44	3.48	192.04	26.95
4	10389	21.46	1.81	–3.30	15.30
8	12513	24.78	1.22	33.88	19.85
16	4032	22.64	2.59	–86.30	26.14
15	8487	29.00	1.62	12.68	18.77
20	6280	29.88	3.65	–64.09	32.79
11	7954	26.09	3.43	108.80	29.83
18	4702	34.03	2.75	47.00	41.30
21	3654	29.65	6.13	249.18	61.67

Fig. 8. Map and classification of anomalous magnetic and gravity fields.

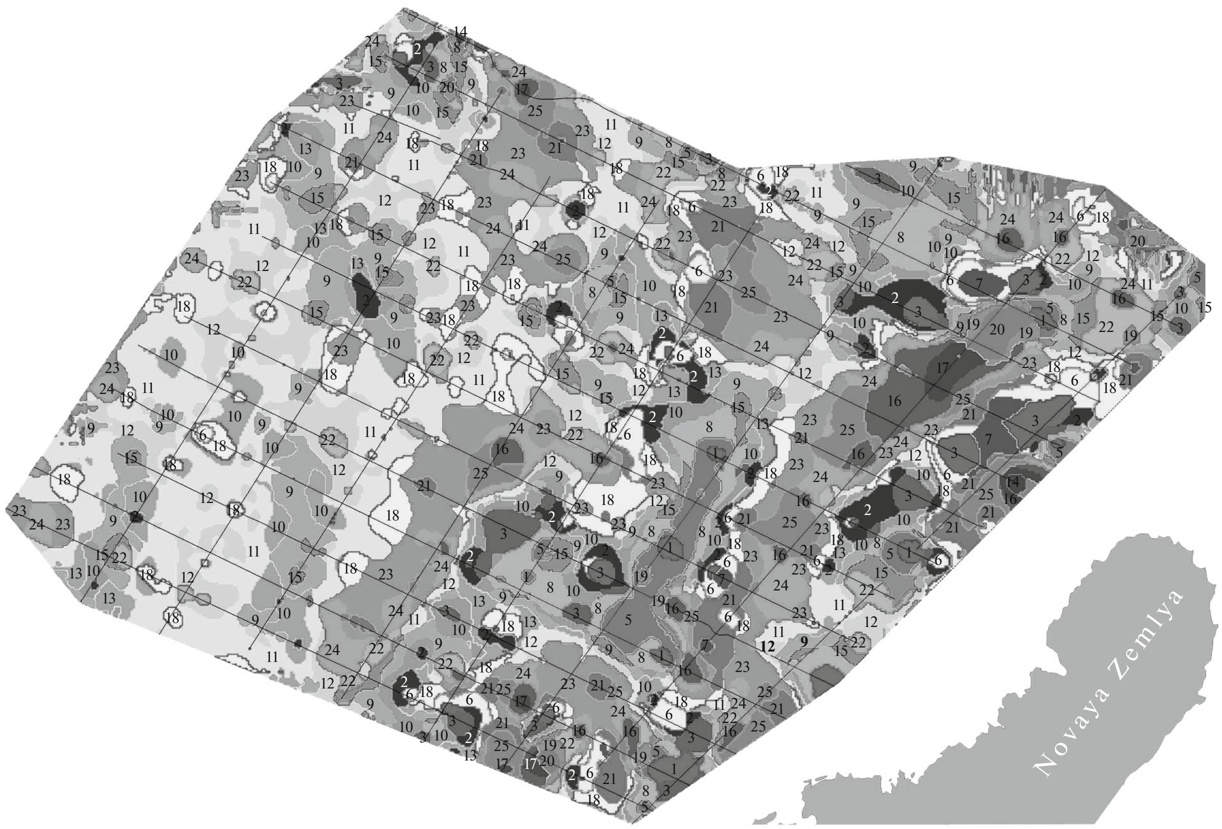

No.	Number of points	Local component of gravity field, mGal		Local component of magnetic field, nT	
		Mean value	Standard deviation	Mean value	Standard deviation
11	109613	0.01	0.03	–0.03	0.57
13	9417	–0.12	0.06	–3.96	1.84
10	5329	–0.38	0.08	–3.44	2.44
4	4200	–0.28	0.11	–12.44	3.56
3	1222	–0.33	0.20	–34.42	8.18
2	2139	–0.76	0.23	–9.54	4.27
12	11819	0	0.06	3.70	1.38
9	8104	–0.19	0.06	1.56	1.65
15	4660	–0.28	0.09	7.57	2.68
8	4324	–0.62	0.13	2.84	2.49
19	920	–0.21	0.25	24.98	5.19
20	684	–0.19	0.28	46.71	5.80
5	2534	0.69	0.14	13.05	4.06
1	799	–1.35	0.35	7.53	11.76
18	9252	0.09	0.09	–6.40	2.33
6	3136	0.05	0.15	–17.75	3.74
23	11992	0.30	0.10	–1.21	2.23
21	4808	0.50	0.21	–10.87	4.19
7	1114	0.41	0.24	–34.22	8.55
22	4314	0.02	0.10	11.53	3.20
24	7690	0.27	0.10	5.88	2.50
25	4033	0.85	0.39	4.54	6.60
16	2803	0.55	0.23	18.93	4.46
17	818	0.74	0.53	41.08	7.92
14	84	0.52	0.43	78.09	12.24

Fig. 9. Map and classification of local components of magnetic and gravity fields.

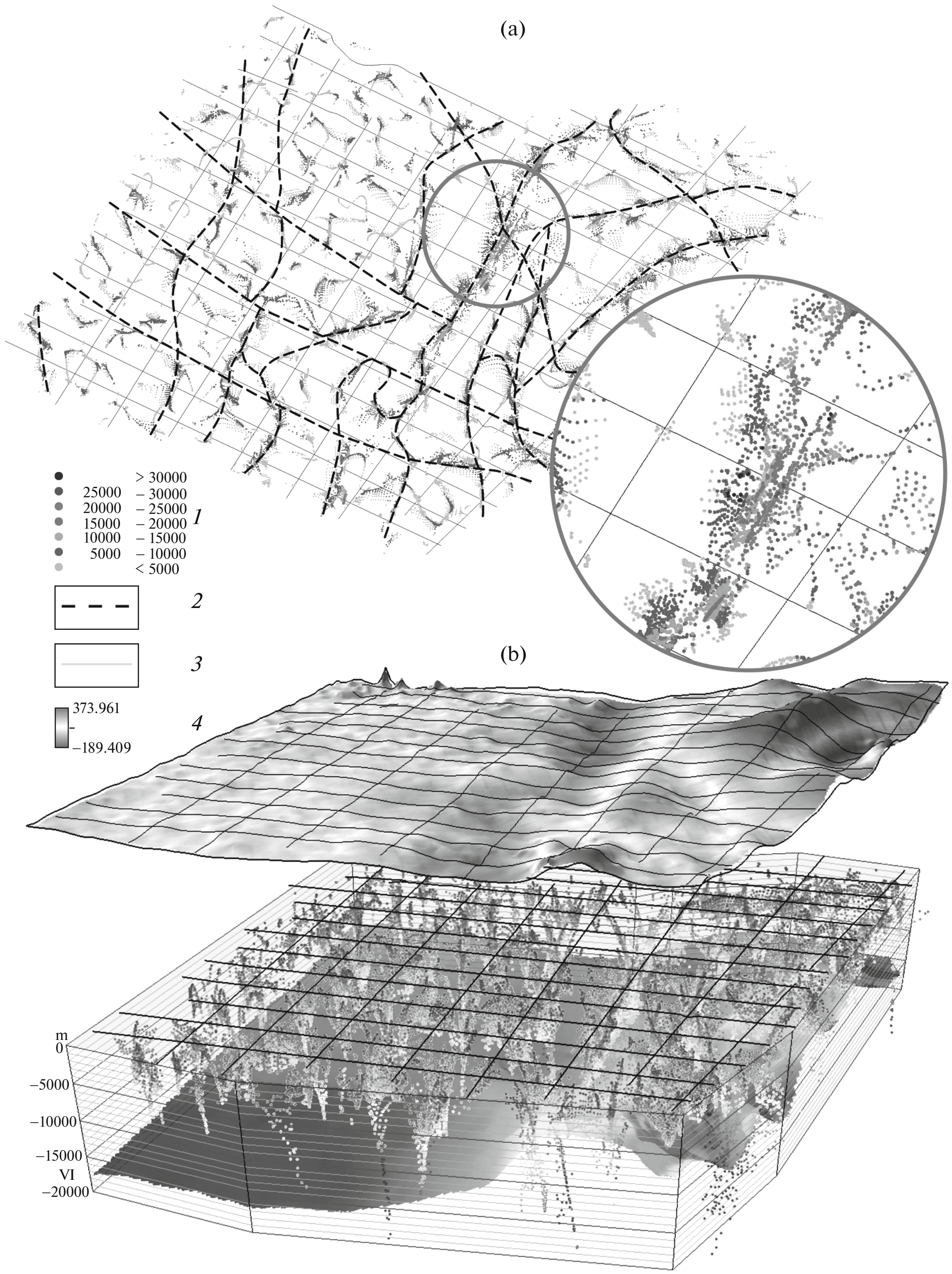

Fig. 10. Positions of special points in geomagnetic model of northeastern Barents Sea shelf: (a) schematic of structural–tectonic faults from magnetometric data, (b) spatial distribution of special points of magnetic field. Arbitrary notes: (*1*) color chart of Eulerian points distribution on depth, m; (*2*) structural–tectonic faults; (*3*) 2D SRM–CDP profiles; (*4*) anomalous magnetic field, nT.

the bottom of the borehole, since the borehole has very unordinary subvertical intrusive bodies (dikes) with minimal displacement amplitudes, seen in the seismic section as columnlike wave anomalies. A characteristic feature of these anomalies is a chaotic seismic record within each "column" and no reflectors traced at their boundaries. Columnlike anomalies were correlated between profiles and formed elongated (up to 100 km) lineaments expressed in the relief as NW-oriented tectonic benches (Fig. 11).

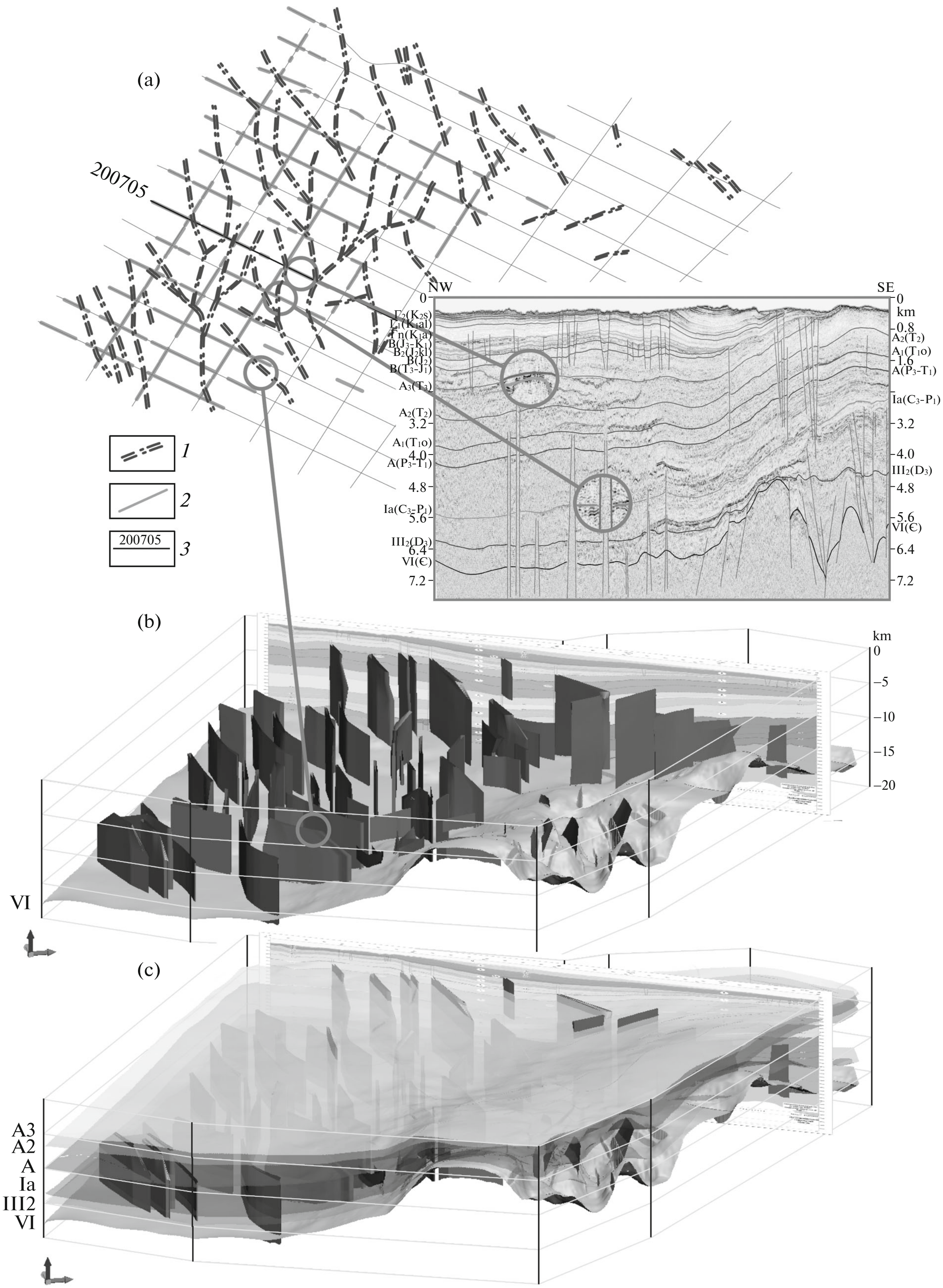

Fig. 11. Distribution area of α-group reflectors: (a) schematic map showing distribution of α-group reflectors in Upper Triassic part of section; (b) spatial model of α-group reflectors identified at VI reflecting horizon, which is a crystalline basement surface; (c) level of α-group reflectors identified from VI to A-A2-A3 horizons, including Paleozoic and Triassic parts of sedimentary cover. Arbitrary notes: (*1*) columnlike anomalies i wave field, interpreted as magmatic conduits (dikes); (*2*) α-group reflectors attributed to layered igneous intrusions (dolerite sills); (*3*) 2D SRM–CDP profiles.

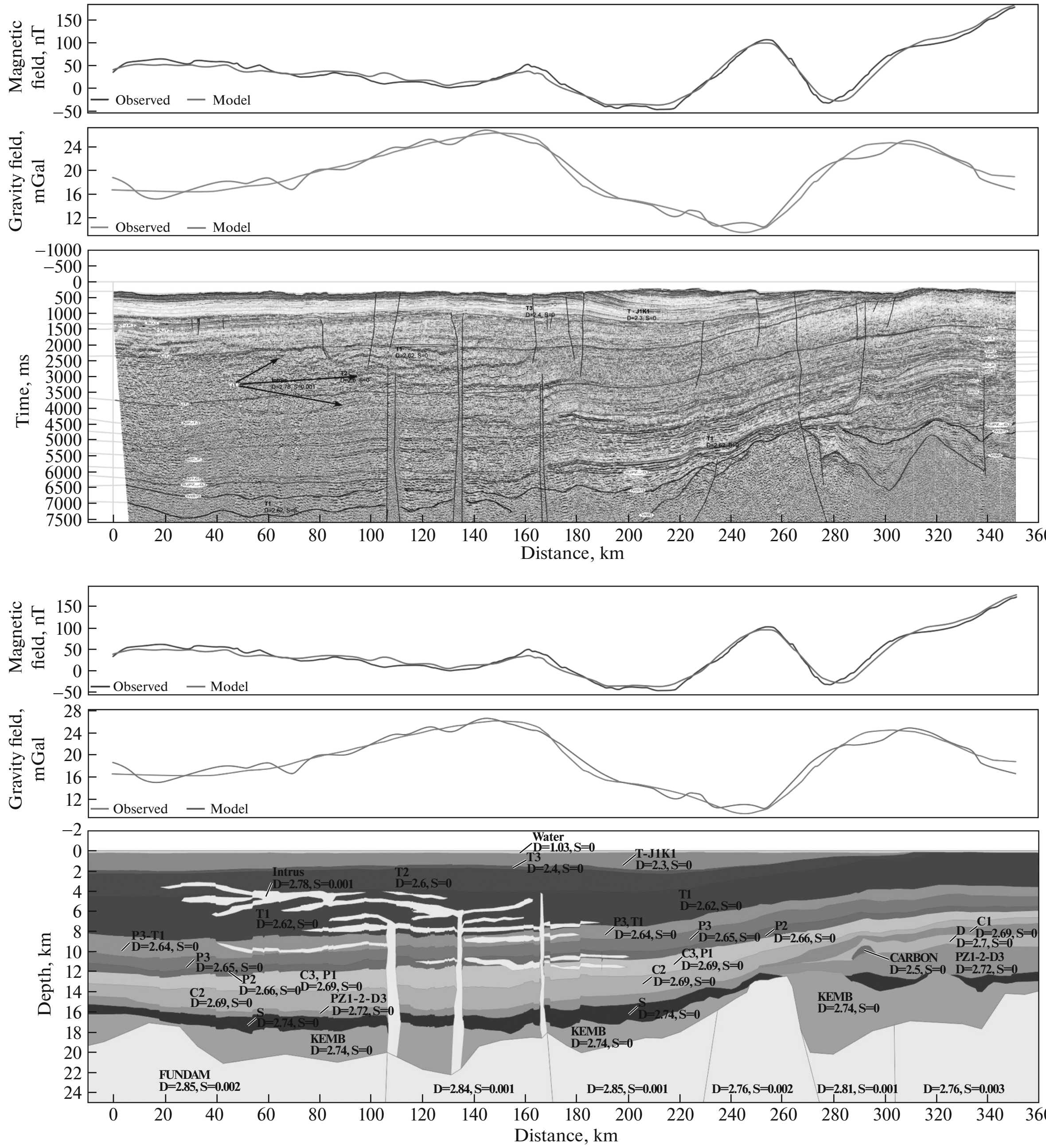

Fig. 12. Geological and geophysical section (profile 200705) based on results of potential field modeling. Location of this section is shown in Fig. 11.

As a result, we obtained a block model where each block had the respective assigned density value.

Using the Neif–Drake algorithm [31], we calculated the seismic wave velocities for each block (Table 1). Using the recalculation algorithm from the GM-SYS module of the OASIS MONTAJ software [38], we recalculated the seismic section to the depth section.

The obtained gravimagnetic effect was compared to the observed magnetic and gravity fields. With the specified geometry of block boundaries and their properties, we obtained a model whose gravimagnetic effect showed the best fit to the observed fields under the assumption of constant physical parameters in any given model block (Fig. 12).

The distribution of the physical parameters makes the model boundaries quite conditional, because variations in these parameters within blocks can be up to 15–20%. The errors related to approximation of the real 3D geological setting can be up to 15% for a given distribution of model blocks. In this respect, there was no need to attain a complete fit between the model and observed fields, with residual differences being 3 mGal

Table 1. Parameters of blocks along profile 200705

Layer	Velocity, m/s	Density, g/cm^3
C1	5873.04	2.69
C2	5873.04	2.69
C3, P1	5873.04	2.69
CARBON	4767.22	2.5
T1	5510.77	2.62
D	5921.31	2.7
FUNDAM	6365.83	2.8
Intrus	6365.83	2.8
KEMB	6195.63	2.76
P1	5823.97	2.68
P2	5723.28	2.66
P3	5671.59	2.65
P3-T1	5618.97	2.64
PZ1-2-D3	6015.55	2.72
S	6106.92	2.74
T-J1K1	3391.68	2.3
T1	5510.77	2.62
T2	5398.4	2.6
T3	4047.7	2.4
Water	1450	1.03

and 20 nT for the gravity and magnetic fields, respectively. These differences were caused mainly by real inhomogeneities of the deep structure, which were not in any way reflected in the seismic data and were not taken into consideration in models.

Generalization of the available data on the structures of the sedimentary cover and upper basement and the use of novel results from interpreting the potential fields allow the conclusion that the basement has a heterogeneous structure and multiphase tectonomagmatic activity, which began at the very end of the Paleozoic but became especially noticeable in the Triassic. Downwarping of the basement and intensification of extensional stresses led to the intrusion of multiple gabbro-dolerite dikes, which formed benchlike NW-oriented structures. According to the drilling results, these intrusions had a long-term history, because gabbro and dolerite layers were recovered even in the sedimentary cover.

As a result of potential field interpretation and analysis of the available geological data, we can state that reconstruction of the basement took place in the northeastern Barents Sea during the entire Triassic on a background of rapid downwarping and intensive sedimentation.

CONCLUSIONS

Based on the modeling results, we can conclude the following.

(1) The calculated thickness of the sedimentary cover in the East Barents megatrough is 18–20 km.

(2) According to the seismic survey data, intrusions (dolerite dikes and sills) within the sedimentary cover form columnlike anomalies in the wave field in the upper part of the sedimentary cover (the upper rim is at a depth of about 3–4 km, with layered intrusions 500–1500 m thick). The intrusions are located primarily in Upper Permian–Triassic deposits.

(3) The gravity effect from intrusive bodies can be up to 10 mGal, with a dolerite density of 2.78 g/cm^3, which contributes substantially to the observed gravity field and indicates significant extents of Late Permian–Triassic magmatism. The columnlike anomalies, which are clearly identified in the wave field, are most likely long-lived structures coinciding with fault zones and corresponding to conduits of magma material.

(4) Basement rocks are characterized by a block structure with different densities (from 2.76 to 2.85 g/cm^3) and magnetization (from 100 to 300 × 10^{-5} SI).

(5) The block boundaries usually correspond to tectonic faults, which are also clearly identified when interpreting the areal data.

Our comprehensive analysis of potential fields jointly with the seismic survey data, modeling of tectonic elements using modern algorithms and software, zoning in terms of geophysical data, and modeling of potential fields have allowed us to obtain broader knowledge about the peculiarities of magmatism, petrophysical characteristics, and structural–tectonic organization of the northeastern Barents Sea shelf.

ACKNOWLEDGMENTS

The work was supported by the state budget (project no. 0135-2015-0021) and by the Presidium of the Russian Academy of Sciences (program no. 15).

REFERENCES

1. S. V. Aplonov, G. B. Shmelev, and D. K. Krasnov, "Geodynamics of the Barents–Kara shelf: Geophysical evidence," Geotectonics **30**, 309–326 (1996).
2. *Seas of the Arctic and Russian Far East*, Vol. 5, Pt. 1 of *Geology and Mineral Resources of Russia*, Ed. by I. S. Gramberg, V. L. Ivanov, and Yu. E. Pogrebitskii (VSEGEI, St. Petersburg, 2004) [in Russian].
3. *Barents Shelf Plate*, Vol. 196 of *Tr. Sevmorgeologiya*, Ed. by I. S. Gramberg (Nedra, Leningrad, 1988) [in Russian].
4. N. A. Bogdanov, "Tectonics of the Arctic Ocean," Geotectonics **38**, 166–181 (2004).
5. V. I. Bondarev, Yu. P. Ershov, and B. S. Ipatov, "Tectonic evolution of the Northern Island of Novaya Zemlya," in *Geology and Stratigraphy of Novaya Zemlya* (Sevmogeologiya, Leningrad, 1979), pp. 5–17.
6. M. L. Verba, "Crustal extension in the Barents Sea shelf," in *Natural Conditions and Resources of Northern Seas* (Geogr. O-vo SSSR, Leningrad, 1977), pp. 28–32.
7. *Geological Structure of USSR and Regularities of Mineral Resources Distribution*, Vol. 9: *Soviet Arctic Seas*, Ed. by

I. S. Gramberg and Yu. E. Pogrebitskii (Nedra, Leningrad, 1984) [in Russian].

8. *State Geological Map of Russian Federation, Scale 1 : 1000000 (New Series). Sheet R-38-40, Kolguyev. Explanatory Note*, Ed. by B. G. Lopatin (VSEGEI, St. Petersburg, 2003) [in Russian].
9. I. S. Gramberg, "The Barents Sea Permo–Triassic paleorift and its importance to the problem of oil and gas potential of the Barents–Kara Platform," Dokl. Earth Sci. **353**, 198–200 (1997).
10. I. S. Gramberg, Yu. N. Kulakov, Yu. E. Pogrebitskii, and D. S. Sorokov, "Arctic petroleum-bearing superbasin" in *Petroleum-Bearing Potential and of the World Ocean* (PGO Sevmorgeologiya, Leningrad, 1984), pp. 7–21.
11. I. S. Gramberg, V. I. Bondarev, N. N. Sobolev, and L. A. Daragan-Sushchova, "Reconstruction of the geological structure of the eastern Barents Sea region from the comprehensive analysis of geological-geophysical data," in *Russian Arctic: Geological History, Minerageny, and Geology* (VNIIOkeangeologiya, St. Petersburg, 2002), pp. 193–201.
12. V. S. Zhuravlev and M. E. Raaben, "Hypothesis about the Barentia in the light of the modern data," in *Tectonics of the East European Platform and Its Framing* (Nauka, Moscow, 1975), pp. 75–92.
13. L. P. Zonenshain and L. M. Natapov, "Tectonic evolution of the Arctic," in *Topical Problems of Oceanic and Continental Tectonics* (Nauka, Moscow, 1987), pp. 31–56.
14. O. N. Zuikova and E. S. Mirolyubova, "Formation conditions and petroleum-bearing perspectives of the Lower Paleozoic deposits," in *Geological-Geophysical Characteristics of the Arctic Region Lithosphere* (VNIIOkeangeologiya, St. Petersburg, 2006), Vol. 6, pp. 64–75.
15. A. M. Karasik, "Magnetic anomalies of the Gakkel Ridge and origin of the Eurasia superbasin, Arctic Ocean," in *Geophysical Survey Methods in the Arctic* (NIIGA, Leningrad, 1968), Vol. 5, pp. 9–19.
16. E. A. Korago and T. N. Timofeeva, *Magmatism of Novaya Zemlya*, Vol. 209 of *Tr. NIIGA-VNIIOkeangeologiya* (St. Petersburg, 2005) [in Russian].
17. *Soviet Arctic Seas*, Vol. 9 of *Geological Structure of USSR and Regularities of Mineral Resources Distribution* (Nedra, Leningrad, 1984) [in Russian].
18. *Novaya Zemlya and Vaigach Island: Geological Structure and Minerageny*, Vol. 205 of *Tr. NIIGA-VNIIOkeangeologiya* (St. Petersburg, 2004) [in Russian].
19. *Islands of Soviet Arctic*, Vol. XXVI of *Geology of USSR* (Nedra, Moscow, 1970) [in Russian].
20. A. D. Pavlenkin, "Caledonian rifting in the Barents Sea shelf," in *Geological Structure of the Barents–Kara Shelf* (PGO Sovmorgeologiya, Leningrad, 1985), pp. 29–33.
21. A. P. Piskaryov, *Petrophysical Models of the Earth's Crust in the Arctic Ocean*, Vol. 203 of *Tr. NIIGA-VNIIOkeangeologiya* (St. Petersburg, 2004) [in Russian].
22. Yu. E. Pogrebitskii, "Geodynamic system of the Arctic Ocean and its structural evolution," Sov. Geol., No. 12, 3–28 (1976).
23. T. S. Sakulina, M. L. Verba, N. M. Ivanova, Yu. V. Roslov, and I. V. Belyaev, "Deep structure of the northern Barents–Kara region along the 4-AR profile," in *Proceedings of the 7th Forum "Fuel and Energy Complex of Russia"* (St. Petersburg, 2007), pp. 371–374.
24. *Tectonic Map of the Barents Sea and Northern European Part of Russia, Scale 1 : 2500000*, Ed. by N. A. Bogdanov V. E. Khain, V. I. Bogatskii, S. L. Kostyuchenko, B. V. Senin, E. V. Shipilov, and S. F. Sobolev (PKO Kartografiya, Moscow, 1996).
25. N. I. Timonin, *Pechora Plate: Geological Evolution in the Phanerozoic* (Ural. Otd. Ross. Akad. Nauk, Yekaterinburg, 1998) [in Russian].
26. V. I. Ustritskii, "Tectonic nature of the Barents–North Kara megatrough," in *Problems of Petroleum-Bearing Potential of the World Ocean* (Moscow, 1989), pp. 182–191.
27. V. I. Ustritskii and A. I. Khramov, "Geological evolution of the Arctic from the plate tectonic point of view," in *Soviet Arctic Seas*, Vol. 9 of *Geological Structure of USSR and Regularities of Mineral Resources Distribution* (Leningrad, 1984), pp. 235–265.
28. M. D. Khutorskoi, V. R. Akhmedzyanov, A. V. Ermakov, Yu. G. Leonov, L. V. Podgornykh, B. G. Polyak, E. A. Sukhikh, and L. A. Tsybulya, *Geothermy of the Arctic Seas* (GEOS, Moscow, 2013) [in Russian].
29. M. D. Khutorskoi and B. G. Polyak, "Role of radiogenic heat generation in surface heat flow formation," Geotectonics **50**, 179–195 (2016).
30. L. A. Tsybulya, V. G. Levashkevich, O. A Zalivchii, and I. V. Shkola, "Heat flow in the Kara Sea and on its islands," Geol. Geofiz., No. 11, 93–98 (1994).
31. B. K. Bhattacharya, "Continuous spectrum of the total magnetic field anomaly due to a rectangular prismatic body," Geophysics **31**, 97–121 (1966).
32. J. P. Burg, *Unpublished Doctoral Dissertation* (Stanford Univ., 1975).
33. V. K. Gupta and F. S. Grant, "Mineral exploration aspects of gravity and aeromagnetic survey in Sudbury-Cobalt area, Ontario," in *The Utility of Regional Gravity and Magnetic Anomaly Maps*, Ed. by W. J. Hinze (1985), pp. 392–411.
34. I. N. Macleod, S. Vierra, and A. C. Chaves, "Analytic signal and reduction-to-the-pole in the interpretation of total magnetic field data at low magnetic latitudes," in *Proceedings of the Third International Congress of the Brazilian Geophysical Society, Rio de Janeiro, Brazil, 1993.*
35. J. H. McClellan and H. Nawab, "Complex General-N Winograd Fourier Transform Algorithm (WFTA)," in *Programs for Digital Signal Processing* (IEEE Press, 1979), pp. 1.7-1–1.7-10.
36. A. Spector and F. S. Grant, "Statistical models for interpreting aeromagnetic data," Geophysics **35**, 293–302 (1970).
37. S. Winograd, "On computing the discrete Fourier transform," Math. Comput. **32**, 175–199 (1978).
38. Oasis montaj, Geosoft Software. http://www.geosoft.com/ru. Accessed March 5, 2017.
39. COSCAD-3D software complex for spectral correlation analysis of data. http://coscad3d.ru/. Accessed March 5, 2017.

Reviewer: A.S. Baluev

Translated by N. Astafiev